Signal-Flow-Graph Analysis of Weakly Nonlinear Microwave Circuits Around a Large-Signal Operating Point

Shuhei Amakawa, *Member, IEEE*, Ryotaro Sugimoto, Korkut Kaan Tokgoz, *Member, IEEE*,
Sangyeop Lee, *Member, IEEE*, Hiroyuki Ito, *Member, IEEE*, and Ryoko Kishikawa

Abstract— A signal flow graph (SFG) representation of small-signal responses of nonlinear microwave circuits around a large-signal operating point is developed using the X-parameters. It is shown that, unlike the SFGs for linear circuits, negative-frequency nodes need to be included explicitly. The development elucidates the circuit-operational meaning of the elusive T-type small-signal X-parameters, which represent the interaction between positive- and negative-frequency components. As an example, such an SFG is used to derive a closed-form expression of the output power of an amplifier as a function of the load reflection coefficient. It is then used to plot approximate load-pull power contours. The result is consistent with the expressions of the optimum load reflection coefficient derived by Root et al. (EuMIC 2017) and power contours derived by Peláez-Pérez et al. (TMTT 2013). SFGs provide an alternative systematic means to derive closed-form expressions in terms of X-parameters and gain illuminating insights into the workings of weakly nonlinear circuits.

Index Terms— Frequency mixing, intermodulation distortion, polyharmonic distortion model, S-functions, uncertainty propagation, X-parameters.

I. INTRODUCTION

THE wide availability of nonlinear microwave simulators has greatly facilitated the design of nonlinear circuits. Such simulators are especially useful for iterative parameter optimization at the later stages of design. Nevertheless, analytic or semianalytic design approaches could help in the initial phase of design. (Semi)analytic results could provide design insights [1] and reasonable initial guesses for nonlinear optimization, thereby speeding up its convergence to a good solution. The celebrated load-pull theory based on

the dc loadline [2], [3], for example, provided a remarkable insight into power amplifier (PA) design. In contrast, numerical simulation results, albeit very valuable, might not be particularly insightful [1].

As regards linear circuits, various useful closed-form expressions have been derived in terms of S-parameters. S-parameters go very well with the signal flow graphs (SFGs) [4], [5]. SFGs offer a systematic means to derive closed-form expressions in terms of S-parameters [6], [7], [8] and are frequently used especially in metrology.

Nonlinear scattering functions and their derivatives [9], [10] can be regarded as a natural extension of S-parameters. "X-Parameters"[1] [11], [12] is one persuasion that considers only first-order derivatives. Similar frameworks to X-parameters include "S-functions" [12], [13], [14]. Although X-parameters can be black-box models of nonlinear devices and circuits [15], [16], applications of X-parameters toward analytic design or modeling of nonlinear circuits and devices have recently made great progress [17], [18], [19], [20], [21], [22], [23], [24], [25], [26], [27]. Dunsmore [28, p. 427] described the findings of [22] as "a breakthrough." This was, perhaps, an indication of how little we had actually known about the meaning of X-parameters. Better understanding could potentially lead to more ideas for design or modeling. The contribution of this article is to demonstrate how SFGs can be adapted to the X-parameter framework. SFGs will be shown to provide an alternative means to derive useful closed-form expressions, just as in the linear case. More importantly, SFGs provide an intuitive picture of the operation of weakly nonlinear circuits, not readily available from purely algebraic treatment or from nonlinear circuit simulation.

The rest of this article is organized as follows. Section II briefly describes X-parameters with a single fundamental tone, together with the notation used in this article (slightly different from that in [11]) and simplifying assumptions made. Section III introduces SFGs for weakly nonlinear circuits operating around a large-signal operating point (LSOP) [9], [11] and highlights new insights gained through looking at SFGs. Section IV presents an application example, in which approximate load-pull power contours of an amplifier are plotted using a closed-form expression. The derived expression is shown to be consistent with predictions by existing theories [20], [22] and could be useful for making quick estimates. Finally, Section V summarizes the main results and discusses prospects. In the Appendix, detailed graphical derivations of some closed-

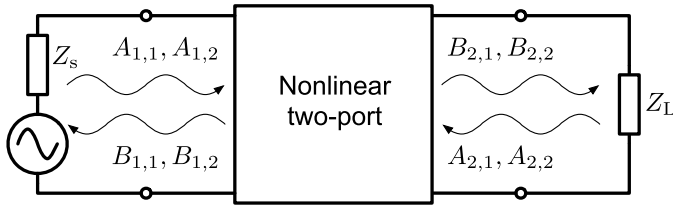[1]"X-Parameters" is a registered trademark of Keysight Technologies, Inc.

Fig. 1. Time-invariant nonlinear two-port. $A_{p,k}$ and $B_{p,k}$ are, respectively, the incoming and outgoing pseudotraveling-wave phasors at port p at the kth harmonic. Z_s is the signal source impedance, and Z_L is the load impedance.

form expressions are given. Also, an SFG-based explanation is given of why the output impedance of a nonlinear amplifier depends on the load impedance. How load-dependent X-parameters [11], [15] could be accommodated to SFGs is also discussed.

II. X-PARAMETERS WITH ONE FUNDAMENTAL TONE

Let us consider a time-invariant nonlinear two-port (see Fig. 1). In the following, we will consider only a single fundamental tone, ω_0 (>0), and mainly the first two harmonics (ω_0 and $2\omega_0$) to avoid complication. We will not explicitly consider the dc response functions, $X^{(\text{dc})}(\cdot)$ [11].

In a large-signal periodic steady state, which comprises large-signal stimuli and large-signal responses, the outgoing pseudotraveling-wave [29], [30] phasor, $B_{p,k}$, at physical port p with a harmonic number k can be written using a phase-normalized nonlinear scattering function (or B-type X-parameter [31]) $X^{(B)}_{p,k}(\cdot)$ as follows [11]:

$$B_{p,k} = X^{(B)}_{p,k}\big(|A_{1,1}|, A_{1,2}\Phi^{-2}, A_{2,1}\Phi^{-1}, A_{2,2}\Phi^{-2}\big)\Phi^k \quad (1)$$

where $A_{q,l}$ are the incoming pseudotraveling-wave phasors at physical port q with a harmonic number l, and

$$\Phi \triangleq e^{j\angle A_{1,1}} \quad (2)$$

is the so-called twiddle factor [12]. "$\triangleq$" in (2) denotes equality by definition. The 2-tuples $\{p, k\}$ and $\{q, l\}$ can be regarded as logical port indices.

Following the convention in [11], phasors in this article are root mean square (rms) phasors. In the time domain, $A_{1,1}$, for example, can be written as

$$A_{1,1}(t) = \sqrt{2}|A_{1,1}| \cos\big(\omega_0 t + \angle A_{1,1}\big)$$
$$= \sqrt{2}\text{Re}\big(A_{1,1}e^{j\omega_0 t}\big) = \frac{A_{1,1}e^{j\omega_0 t} + A^*_{1,1}e^{-j\omega_0 t}}{\sqrt{2}} \quad (3)$$

where $A_{1,1}$ is the phasor at time $t = 0$, and $A^*_{1,1}$ is its complex conjugate. Equation (3) indicates that a sinusoidal signal is composed of the positive-frequency component $A_{1,1}e^{j\omega_0 t}$ and the negative-frequency component $A^*_{1,1}e^{j(-\omega_0)t}$ [10], [12], [32], [33], as shown in Fig. 2.

Suppose now that port 1 of the two-port (see Fig. 1) is driven by a signal source with a signal-source impedance Z_s that is equal to the reference resistance[2] R_{ref} (>0), which typically is 50 Ω. Suppose further that the load impedance Z_L, too, equals

Fig. 2. Visualization of $A_{1,1}(t)$ in (3) on the complex plane. $A_{1,1}$ and $A^*_{1,1}$ are rms phasors at $t = 0$.

R_{ref}. Then, the source and load reflection coefficients at the kth harmonic

$$\Gamma_{s,k} = \frac{Z_{s,k} - R_{\text{ref}}}{Z_{s,k} + R_{\text{ref}}} \quad (4)$$

$$\Gamma_{L,k} = \frac{Z_{L,k} - R_{\text{ref}}}{Z_{L,k} + R_{\text{ref}}} \quad (5)$$

become 0. This makes $A_{1,2} = A_{2,1} = A_{2,2} = 0$. We hereafter assume for simplicity that X-parameters are to be obtained at such LSOPs (the "load-independence" assumption[3] [19], [20]) by using a suitable nonlinear network analyzer or a nonlinear microwave simulator. Then, (1) becomes a function of $A_{1,1}$ alone as follows:

$$B^{\text{LSOP}}_{p,k}(A_{1,1}) = X^{(B)}_{p,k}\big(|A_{1,1}|\big)\Phi^k. \quad (6)$$

Now, if, for example, the values of $Z_{s,k}$ and/or $Z_{L,k}$ deviate from R_{ref}, $A_{q,l} = 0$ $((q,l) \neq (1,1))$ and $B_{p,k} = B^{\text{LSOP}}_{p,k}$ will no longer hold.[4] If the nonlinearity of the two-port is weak at a given LSOP, a small deviation from the LSOP can be approximated by linearizing $X^{(B)}_{p,k}(\cdot)$ by first-order Taylor expansion around the LSOP as follows [11, Sec. 5.2.2]:

$$B_{p,k} \simeq B^{\text{LSOP}}_{p,k} + \sum_{q,l}\Bigg[\frac{\partial X^{(B)}_{p,k}}{\partial(A_{q,l}\Phi^{-l})}\Bigg|_{\text{LSOP}} a_{q,l}\Phi^{k-l}$$
$$+ \frac{\partial X^{(B)}_{p,k}}{\partial(A_{q,l}\Phi^{-l})^*}\Bigg|_{\text{LSOP}} a^*_{q,l}\Phi^{k+l}\Bigg] \quad (7)$$

where the derivatives are Wirtinger derivatives [22], [34], and

$$a_{q,l} \triangleq A_{q,l} - A^{\text{LSOP}}_{q,l} \quad (8)$$

is the small deviation of $A_{q,l}$ from the LSOP value $A^{\text{LSOP}}_{q,l}$ ($A^{\text{LSOP}}_{1,1} \neq 0$ and $A^{\text{LSOP}}_{q,l} = 0$ for $(q,l) \neq (1,1)$). The presence of the second term of (8) is essential, especially when $A^{\text{LSOP}}_{q,l} \neq 0$ (considered in Appendix C). If it did not exist, (7) would not be a Taylor expansion. Equation (7) can be

---

[2]In this article, we will consider only positive real reference impedances to avoid possible confusion [30]. We also assume, for simplicity, that R_{ref} is independent of frequency and is common to all ports.
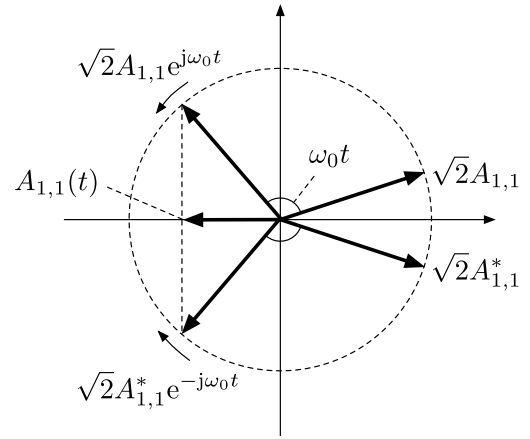
[3]The load-independence assumption is made here just to make the example that follows simple. It is not a requirement for the following development.

[4]An implicit simplifying assumption made here is that the value of $A_{1,1}$ remains constant when $Z_{s,1}$ deviates from R_{ref}, and therefore, the first term of (7) is not affected by the deviation via (6). However, normally, $A_{1,1}$ will be affected by the change in $Z_{s,1}$ according to (15) and (4) if P_{avs} is fixed, thereby shifting the LSOP itself. The assumption has been made to introduce the concept using a one-port as an example in Section III.
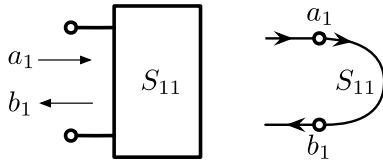
Fig. 3.   SFG (right) of a linear one-port (left).

written in terms of the S-type and T-type small-signal X-parameters [31] as follows:

$$B_{p,k} \simeq B_{p,k}^{\text{LSOP}} \\ + \sum_{q,l} \Big[X_{p,k;q,l}^{(S)} a_{q,l} \Phi^{k-l} + X_{p,k;q,l}^{(T)} a_{q,l}^* \Phi^{k+l} \Big] \quad (9)$$

$$X_{p,k;q,l}^{(S)} \triangleq \left. \frac{\partial X_{p,k}^{(B)}}{\partial (A_{q,l}\Phi^{-l})} \right|_{\text{LSOP}} \quad (10)$$

$$X_{p,k;q,l}^{(T)} \triangleq \left. \frac{\partial X_{p,k}^{(B)}}{\partial (A_{q,l}\Phi^{-l})^*} \right|_{\text{LSOP}}. \quad (11)$$

At the small-signal limit ($|A_{1,1}| \rightarrow 0$), the S-type X-parameters at ω_0 reduce to S-parameters ($X_{p,1;q,1}^{(S)} \rightarrow S_{p,q}$), and the LSOP term of (9) and the T-type X-parameters disappear ($B_{p,k}^{\text{LSOP}} \rightarrow 0$ and $X_{p,k;q,l}^{(T)} \rightarrow 0$) [11]. Since $a_{q,l}^*$ in (9) represents a negative-frequency ($-l\omega_0$) component, $X_{p,k;q,l}^{(T)}$ can be understood as a scattering coefficient from $-l\omega_0$ to $+k\omega_0$ [12]. Taking the complex conjugate of (9), $X_{p,k;q,l}^{(S)*}$ and $X_{p,k;q,l}^{(T)*}$ will represent scattering coefficients from $-l\omega_0$ to $-k\omega_0$ and from $+l\omega_0$ to $-k\omega_0$, respectively. Equation (9) can be rewritten as

$$B_{p,k} \simeq B_{p,k}^{\text{LSOP}} + b_{p,k} \quad (12)$$

where

$$b_{p,k} \triangleq \sum_{q,l} \Big[X_{p,k;q,l}^{(S)} a_{q,l} \Phi^{k-l} + X_{p,k;q,l}^{(T)} a_{q,l}^* \Phi^{k+l} \Big] \quad (13)$$

is the first-order deviation of $B_{p,k}$ from the LSOP value given by (6).

III. SFG FOR NONLINEAR CIRCUIT AROUND LSOP

A. From S-Parameters to Small-Signal X-Parameters

The simplest SFG is that for a linear one-port, as shown in Fig. 3. The SFG has but one branch, and associated with it is the S-parameter S_{11}. The small-signal wave phasors a_1 and b_1 are related to each other by the linear relationship

$$b_1 = S_{11} a_1. \quad (14)$$

In what follows, we will consider the progression from the SFG for a linear one-port (see Fig. 3) to an SFG for a nonlinear one-port or two-port operating near an LSOP, assuming, for simplicity, that $\angle A_{1,1} = 0$, and hence $\Phi = 1$ [see (2)]. Here, we will temporarily forget about the first term of (9) and focus on the linear relationship (13).

Fig. 4(a) shows the first step of the progression, in which the S_{11} in Fig. 3 is replaced by $X_{1,1;1,1}^{(S)}$, and harmonic indices are introduced to the wave phasors. The next step, shown in Fig. 4(b), is the critical step, in which the graph for the negative frequency has been added. The negative-frequency graph need not to be considered explicitly in
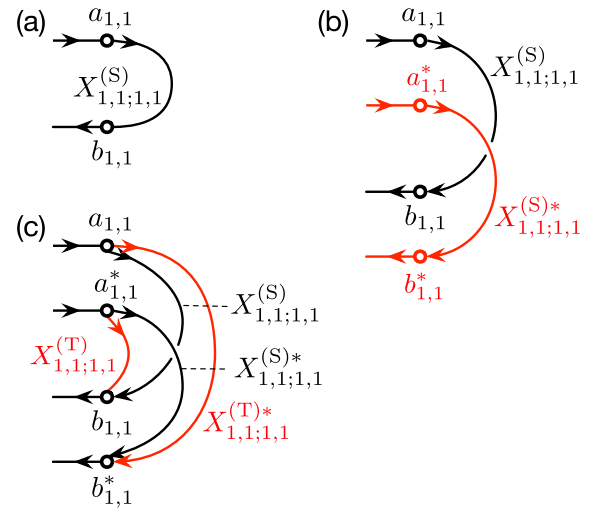

Fig. 4.   Progression to a one-port SFG around an LSOP, not including the contribution from LSOP terms. (a) S-parameter in Fig. 3 is replaced by an S-type X-parameter, and harmonic indices are introduced to wave phasors. (b) Complex-conjugate (negative-frequency) graph is added. (c) Branches connecting positive- and negative-frequency graphs are added.
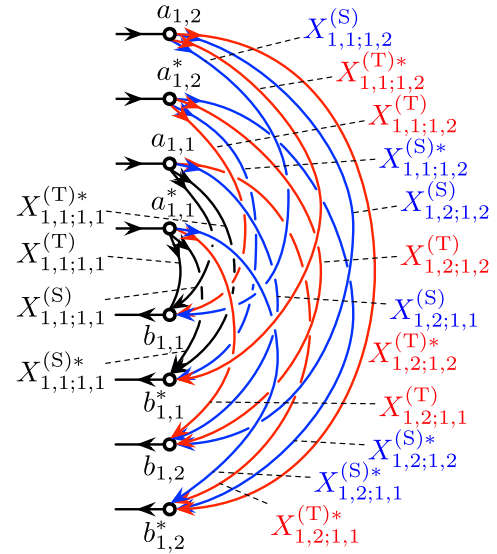

Fig. 5.   Nodes and branches involving harmonic number 2 are added to the SFG in Fig. 4(c). Added S-type X-parameters are shown in blue and T-type X-parameters are shown in red.

the linear case (see Fig. 3) because it is just the complex conjugate of the positive-frequency graph and provides no extra information. However, the presence of $a_{q,l}^*$ in (13) suggests that the negative-frequency graph is needed here [35], [36]. The third step is shown in Fig. 4(c), in which the branches corresponding to $X_{1,1;1,1}^{(T)}$ and $X_{1,1;1,1}^{(T)*}$ are added. Fig. 4(c) visualizes (13) and its complex conjugate for $k = 1$ and $l = 1$. The origin of these branches could be inferred from their role of connecting positive- and negative-frequency nodes as follows. Since the one-port under consideration is nonlinear and is operating in a *large-signal* condition, second-harmonic components, proportional to $e^{\pm j2\omega_0 t}$, are being generated, typically leading to $B_{1,2}^{\text{LSOP}} \neq 0$ and $B_{1,2}^{\text{LSOP}*} \neq 0$. Then, frequency mixing can take place between these $e^{\pm j2\omega_0 t}$ and the incoming fundamental frequency components, $e^{\mp j\omega_0 t}$ (corresponding to $a_{1,1}^*$ and $a_{1,1}$), thereby producing outgoing $e^{\pm j\omega_0 t}$ (corresponding to $b_{1,1}$

TABLE I
INPUT AND OUTPUT FREQUENCIES OF T-TYPE X-PARAMETERS

T-type X-parameters	Output	Explicit input	Implicit input
$X_{p,1;q,1}^{(T)}$, $X_{p,1;q,1}^{(T)*}$	$\pm\omega_0$	$\mp\omega_0$	$\pm2\omega_0$
$X_{p,2;q,1}^{(T)}$, $X_{p,2;q,1}^{(T)*}$	$\pm2\omega_0$	$\mp\omega_0$	$\pm3\omega_0$
$X_{p,1;q,2}^{(T)}$, $X_{p,1;q,2}^{(T)*}$	$\pm\omega_0$	$\mp2\omega_0$	$\pm3\omega_0$
$X_{p,2;q,2}^{(T)}$, $X_{p,2;q,2}^{(T)*}$	$\pm2\omega_0$	$\mp2\omega_0$	$\pm4\omega_0$
$X_{p,k;q,l}^{(T)}$, $X_{p,k;q,l}^{(T)*}$	$\pm k\omega_0$	$\mp l\omega_0$	$\pm(k+l)\omega_0$

TABLE II
INPUT AND OUTPUT FREQUENCIES OF S-TYPE X-PARAMETERS

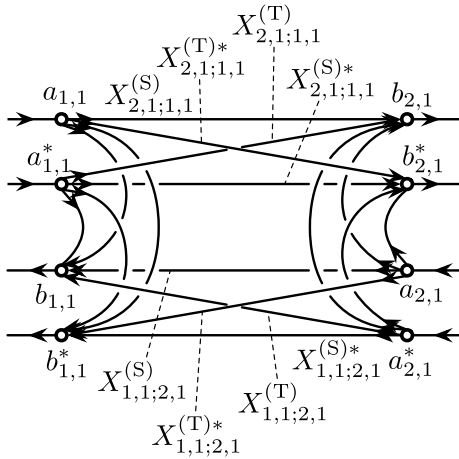| S-type X-parameters	Output	Explicit input	Implicit input
$X_{p,1;q,1}^{(S)}$, $X_{p,1;q,1}^{(S)*}$	$\pm\omega_0$	$\pm\omega_0$	0
$X_{p,2;q,1}^{(S)}$, $X_{p,2;q,1}^{(S)*}$	$\pm2\omega_0$	$\pm\omega_0$	$\pm\omega_0$
$X_{p,1;q,2}^{(S)}$, $X_{p,1;q,2}^{(S)*}$	$\pm\omega_0$	$\pm2\omega_0$	$\mp\omega_0$
$X_{p,2;q,2}^{(S)}$, $X_{p,2;q,2}^{(S)*}$	$\pm2\omega_0$	$\pm2\omega_0$	0
$X_{p,k;q,l}^{(T)}$, $X_{p,k;q,l}^{(T)*}$	$\pm k\omega_0$	$\pm l\omega_0$	$\pm(k-l)\omega_0$

Fig. 6. SFG of a nonlinear two-port around an LSOP, not including the contribution from LSOP terms. The harmonic number is limited to 1.

Fig. 7. Simulated small-signal transmission coefficients $X_{2,k;1,l}^{(T)}$ versus the input available power P_{avs} of a 2-GHz PA (two-stage BJT amplifier) model "RF_PA_CKT" built into ADS at 2 GHz. The slope of $X_{2,k;1,l}^{(T)}$ is given by $(k+l)$ when P_{avs} is sufficiently small.

Fig. 8. Measured small-signal transmission coefficients $X_{2,k;1,l}^{(T)}$ versus the input available power P_{avs} of an amplifier (Mini-Circuits ZFL-11AD+) at 1.8 GHz. Its IP$_{1\text{dB}}$ is about -14 dBm.

and $b_{1,1}^*$). The branches associated with $X_{1,1;1,1}^{(T)}$ and $X_{1,1;1,1}^{(T)*}$ represent part of these *implicit frequency mixing* processes. In this sense, although only harmonic number 1 appears in Fig. 4(c), effects of the second harmonic are included in it to some extent. The implication is that single-tone X-parameters include information about two-tone intermodulation distortion (at the limit of $\omega_1 \rightarrow \omega_0$), which is usually studied using two closely spaced tones, ω_0 and ω_1. This might be a reason why the existing analytic work that used as few as three X-parameters [one large-signal parameter and two small-signal parameters as in (18)] with $k = l = 1$ [17], [18], [19], [20], [21], [22] worked so well.

Fig. 5 shows how nodes and branches involving harmonic number 2 can be added. Explicit frequency upconversion and downconversion branches can now be seen. Input and output frequencies of the eight T-type X-parameters that appear in Fig. 5 are summarized in Table I. In general, the implicit input frequency of $X_{p,k;q,l}^{(T)}$ is $(k+l)\omega_0$. For the sake of completeness, a similar table is presented for the S-type X-parameters (see Table II). $X_{p,2;q,1}^{(S)}$ in Table II is related to harmonic distortion, whereas $X_{p,1;q,2}^{(S)}$ is related to intermodulation distortion. The SFG in Fig. 5 might already look too complicated, but it should at least give an idea of what is happening around an LSOP of
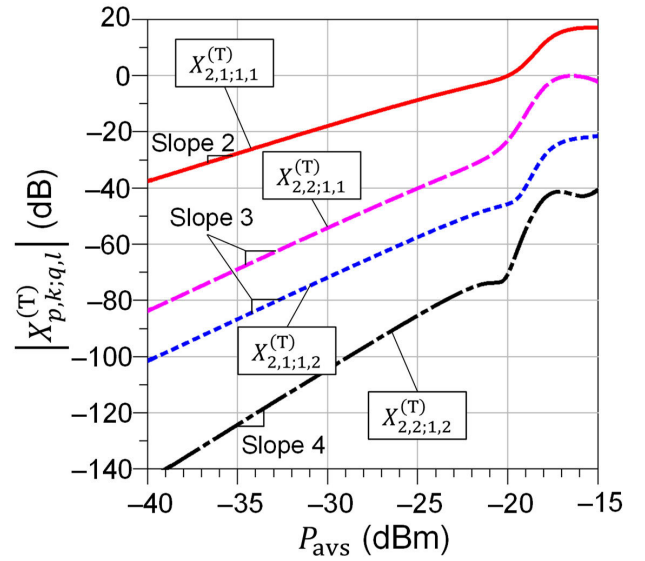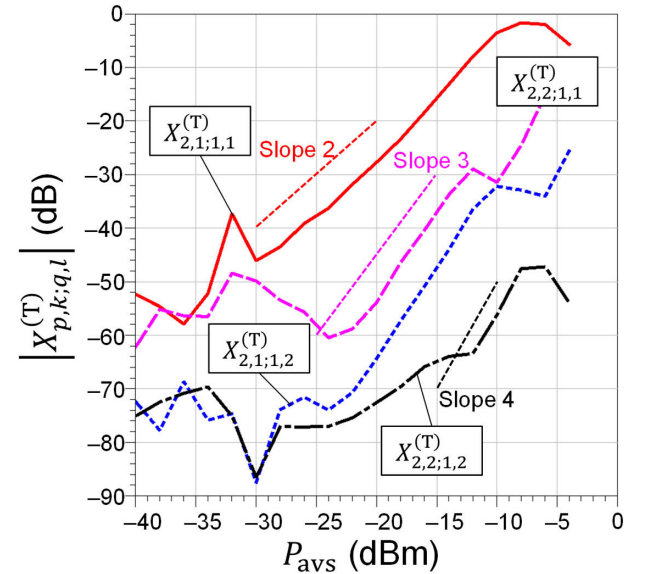
a nonlinear device. Generalization to higher-order harmonics should be obvious. Henceforth, we will limit the harmonic number that we consider to 1 for simplicity unless otherwise stated.

Another generalization over Fig. 4(c) is the addition of physical ports. For instance, Fig. 6 shows an SFG for a two-port. It should be clear from Figs. 5 and 6 that each logical port contributes four nodes. Alternatively, $a_{q,l}^*$ could be understood to be associated with a logical port $\{q, -l\}$ ($l > 0$) [37]. If a harmonic index is allowed to assume a positive or a negative value, then each logical port will contribute to two nodes. This interpretation is more consistent with the linear case.

Fig. 7 shows, in connection with Table I, $|X_{2,k;1,l}^{(T)}|$ of a 2-GHz PA (two-stage BJT amplifier) model "RF_PA_CKT," built into Keysight ADS [31], as a function of the input
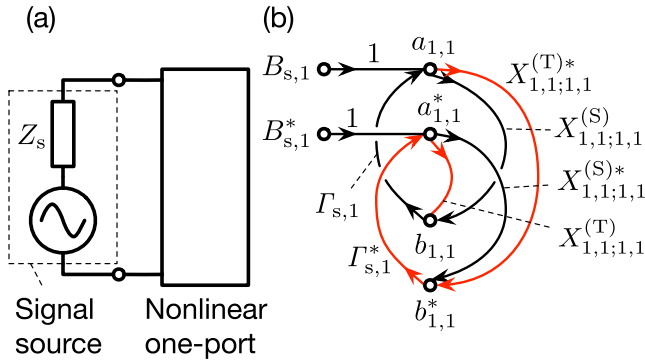
Fig. 9.   (a) Nonlinear one-port driven by a signal source. The source impedance Z_s is assumed to be linear and $\mathrm{Re}(Z_s) > 0$. (b) Corresponding SFG, not including the contribution from LSOP terms. Only X-parameters having harmonic number 1 are considered. Shown in red is the indirect path leading off from $a_{1,1}$ to $b_{1,1}$.

available power, P_{avs}. In general, a plot of $|X_{p,k;q,l}^{(T)}|$ (in dB) versus $|A_{1,1}|$ (in dBm) tends to exhibit a slope of $(k + l)$ at low input power levels because $X_{p,k;q,l}^{(T)}$ is implicitly fueled by the generation of the $(k + l)$th harmonic due to the $(k + l)$th-order nonlinearity. $X_{p,k;q,l}^{(T)}$ is related to the $(k + 2l)$th-order intermodulation distortion (see the second term of (13) and Table I). Fig. 8 shows $|X_{2,k;1,l}^{(T)}|$ of an amplifier (Mini-Circuits ZFL-11AD+), measured with Agilent N5245A. Although the dynamic range of measurement is much more limited than that of numerical simulation (see Fig. 7), the observed slopes are reasonably close to the expected values. Measured $|X_{p,k;q,l}^{(T)}|$ in the literature [9], [11] also exhibited such behavior.

B. Incorporating the LSOP Terms

We now consider how to incorporate into an SFG the first term of (9), which makes (9) an *affine* relationship rather than a linear one. First, consider a one-port driven by a signal source, as shown in Fig. 9(a). How to incorporate a signal source to an SFG is known [6], [8], and the corresponding SFG is shown in Fig. 9(b), which is further progression from Fig. 4(c). The source reflection coefficient, $\Gamma_{s,1}$, at the fundamental frequency is given by (4) with $k = 1$. The R_{ref}-referenced pseudotraveling-wave phasor from the source can be written as [8, p. 19]

$$B_{s,1} = \sqrt{P_{\mathrm{avs}}}\sqrt{\frac{(1 - \Gamma_{s,1}\Gamma_{s,1}^*)(1 - \Gamma_{s,1})}{1 - \Gamma_{s,1}^*}} \qquad (15)$$

where P_{avs} is the available power of the signal source. From Fig. 9(b), $a_{1,1}$ is given by

$$a_{1,1} = B_{s,1} + \Gamma_{s,1}b_{1,1}. \qquad (16)$$

Incidentally, note that Fig. 9(b) lucidly visualizes the known puzzling fact that the small-signal input reflection coefficient, $\Gamma_{\mathrm{in}} = b_{1,1}/a_{1,1}$ in this case, of a nonlinear network is, in general, not equal to $X_{1,1;1,1}^{(S)}$ but depends on the "impedance at your back" [Z_s in Fig. 9(a)]. This is because $X_{1,1;1,1}^{(S)}$ is not the only path that leads off from $a_{1,1}$ to $b_{1,1}$. The other path is $a_{1,1} \to b_{1,1}^* \to a_{1,1}^* \to b_{1,1}$, involving $X_{1,1;1,1}^{(T)*}$, $\Gamma_{s,1}^*$, and $X_{1,1;1,1}^{(T)}$, as shown in red in Fig. 9(b) (see Appendix B for further discussion). There will be more paths if higher harmonic numbers are taken into consideration.
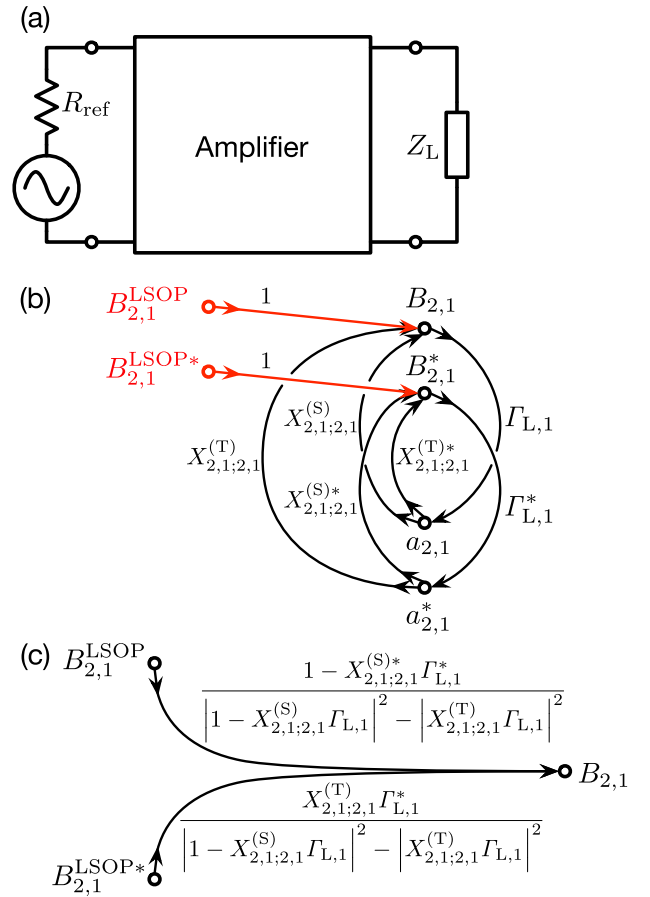

Fig. 10.   (a) Amplifier driven by a signal source with $Z_s = R_{\mathrm{ref}}$, which makes $a_{1,1} = a_{1,1}^* = 0$ in Fig. 6. The load is assumed to be linear. (b) SFG for port 2 of the amplifier around an LSOP. Shown in red are the sources representing the LSOP. (c) Reduced SFG.

Recall at this juncture that a voltage source is a nonlinear circuit element [38]. In this sense, nonlinearity has already been incorporated into the SFG in Fig. 9(b). Comparison of the two affine equations (9) and (16) suggests that the first term of (9) should appear in an SFG as a source node that leads to the $B_{p,k}$ node via a unity-gain branch.

Let us consider the amplifier shown in Fig. 10(a) as an example. The source impedance is $Z_s = R_{\mathrm{ref}}$, and from (4) and (8), $a_{1,1} = a_{1,1}^* = 0$. The amplifier can, therefore, be regarded as a nonlinear one-port as long as its output port is concerned (see Fig. 6). The SFG for the output port of the amplifier is shown in Fig. 10(b). Unlike the ordinary source nodes ($B_{s,1}$ and $B_{s,1}^*$ in Fig. 9(b)), which flow into "a" (incoming wave) nodes, $B_{2,1}^{\mathrm{LSOP}}$ and $B_{2,1}^{\mathrm{LSOP}*}$ flow into "B" (outgoing wave) nodes. The usual graph reduction rules [6], [7] can now be applied to the SFG. The result of eliminating $B_{2,1}^*$, $a_{2,1}$, and $a_{2,1}^*$ is shown in Fig. 10(c). The derivation is given in Appendix A. The output wave phasor, $B_{2,1}(|A_{1,1}|, \Gamma_{L,1}, \Gamma_{L,1}^*)$, therefore, is given by

$$B_{2,1} = \frac{\left(1 - X_{2,1;2,1}^{(S)*}\Gamma_{L,1}^*\right)B_{2,1}^{\mathrm{LSOP}} + X_{2,1;2,1}^{(T)}\Gamma_{L,1}^* B_{2,1}^{\mathrm{LSOP}*}}{\left|1 - X_{2,1;2,1}^{(S)}\Gamma_{L,1}\right|^2 - \left|X_{2,1;2,1}^{(T)}\Gamma_{L,1}\right|^2} \qquad (17)$$

where $\Gamma_{L,1}$ and $B_{2,1}^{\mathrm{LSOP}}$ are given by (5) and (6), respectively. Here, we have, in effect, eliminated $a_{2,1}$ and $a_{2,1}^*$ from the
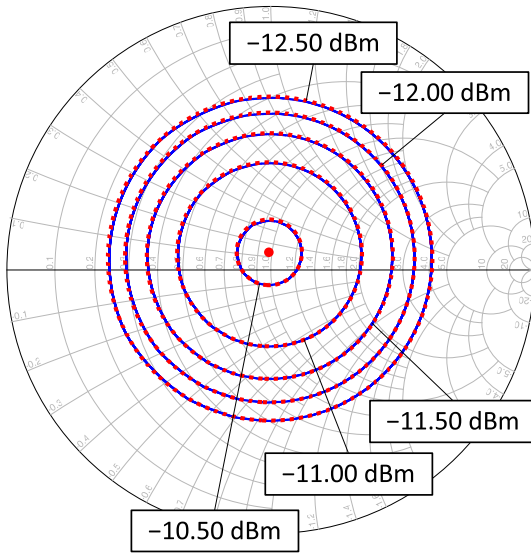
Fig. 11. Output power contours of an amplifier obtained from (20) (red dotted) and from load-pull simulation (blue solid) with the harmonic order set to 7. Contours are drawn at the same power levels in red and blue. The red circular dot is the optimum load reflection coefficient predicted by [22, eq. (10)] and (20). The input (available) power from the source is $P_{\text{avs}} = -40$ dBm, which is a small-signal operating condition.
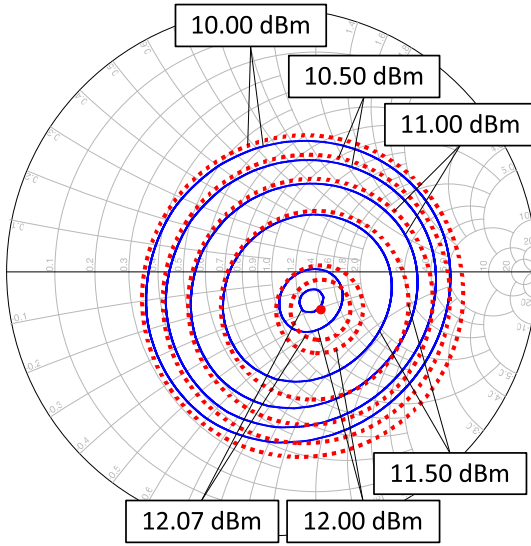

Fig. 12. Same as Fig. 11 except that $P_{\text{avs}} = -16.5$ dBm, which equals $\text{IP}_{1\text{dB}}$.

well-known equation [19], [20], [22] [from (9)]

$$B_{2,1} = B_{2,1}^{\text{LSOP}} + X_{2,1;2,1}^{(S)} a_{2,1} + X_{2,1;2,1}^{(T)} a_{2,1}^*. \tag{18}$$

This is in contrast to the analytic treatment in [19], [20], and [22], in which $a_{2,1}$ and $a_{2,1}^*$ were retained. In our treatment, $a_{2,1}$ can be found from Fig. 10(b) by

$$a_{2,1} = \Gamma_{L,1} B_{2,1}. \tag{19}$$

IV. APPROXIMATE LOAD-PULL POWER CONTOURS

In this section, we show load-pull power contours of an amplifier as a means of checking the logical correctness of (17) and the SFG theory that lead to it. Note, however, that the numerical accuracy offered by *load-independent X-parameters* that we use in the following examples for simplicity is known
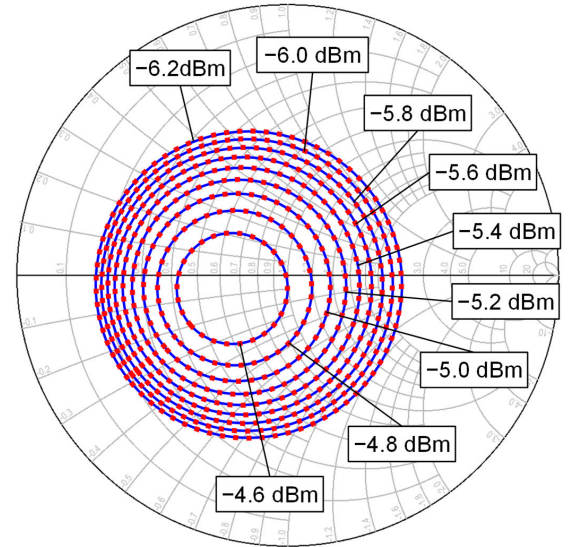

Fig. 13. Load-pull power contours of an amplifier ZFL-11AD+ plotted by using (20) of this article (blue) and [20, eqs. (6)–(18)] (red). The input power is $P_{\text{avs}} = -16$ dBm.
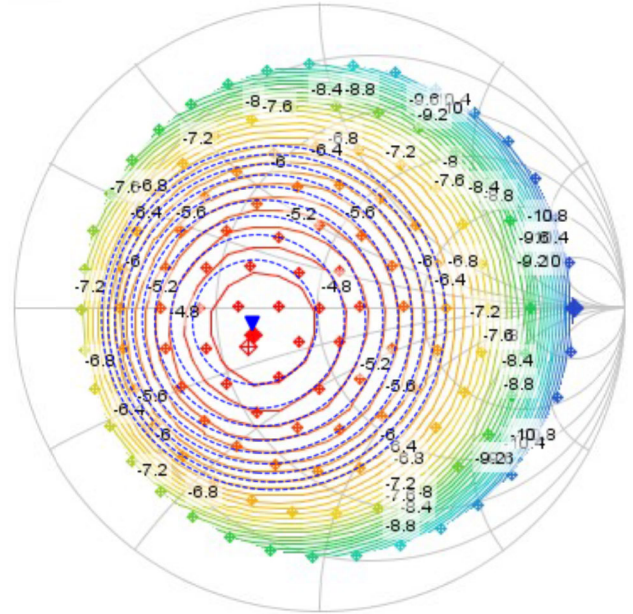

Fig. 14. Measured load-pull power contours of an amplifier ZFL-11AD+ and approximate contours (in blue, same as in Fig. 13) plotted by using (20). The diamond-looking crosses are the measurement points. The input power is $P_{\text{avs}} = -16$ dBm. The large red-filled diamond is the interpolated peak power point from measurement. The blue downward triangle is the theoretically predicted peak power point.

to be limited to a small region on a Smith chart [21] (around the origin in our case). The accuracy could be improved, for example, by shifting the region of good accuracy to a region of interest (e.g., high output power) by making a clever choice of load impedance [20], [24] (although this does not enlarge the region of good accuracy), by making X-parameters load-dependent [11], [15] (at the cost of long measurement time), by considering higher-order derivatives [39], [40], and/or by using more sophisticated extrapolation than Taylor expansion [41]. However, since pursuing numerical accuracy is not the purpose of this article, we just use load-independent X-parameters with a fixed load impedance of 50 Ω in the following.
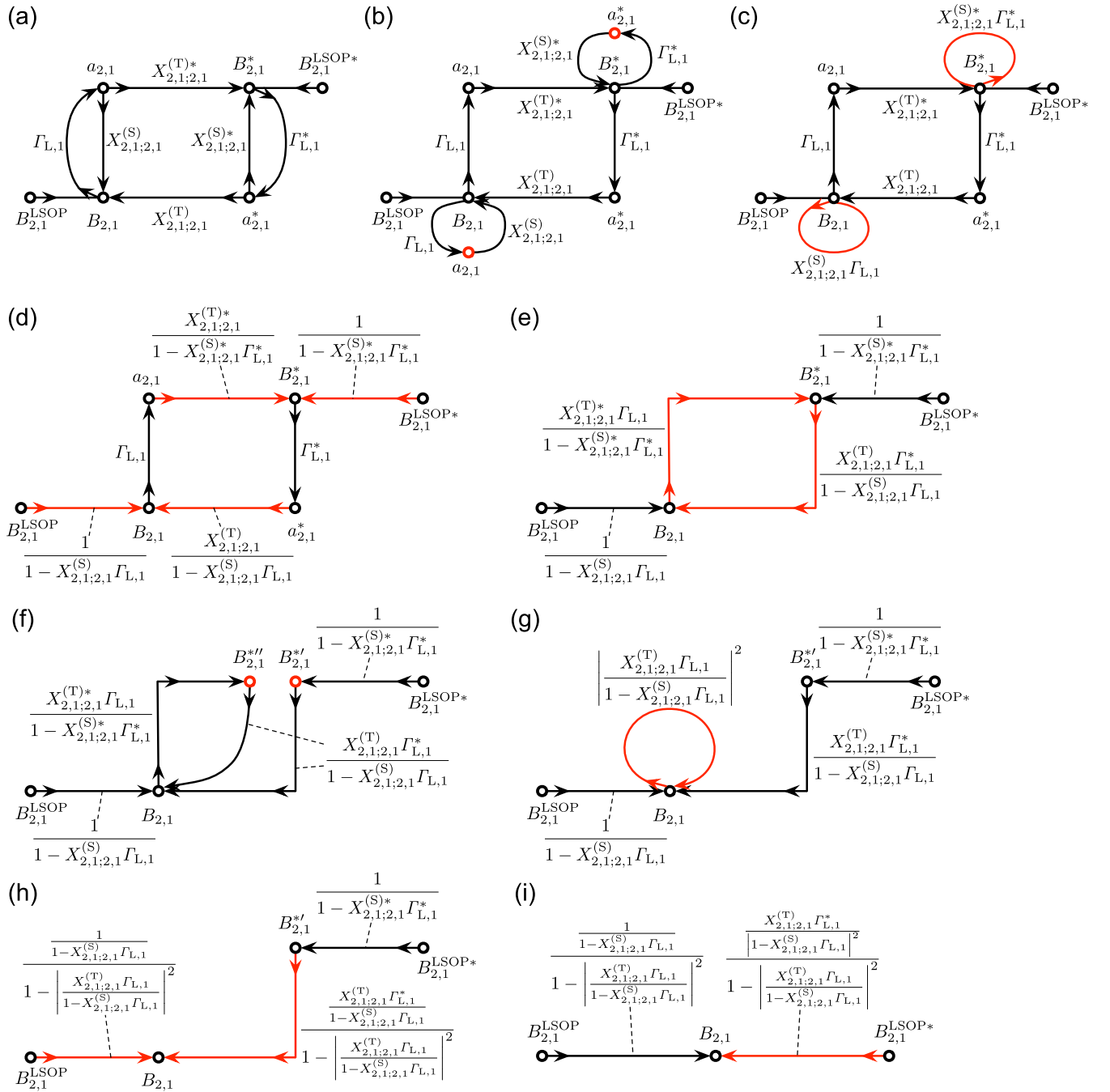
Fig. 15. Step-by-step derivation of the SFG in Fig. 10(c). (a) Redrawn version of the SFG in Fig. 10(b). (b) $a_{2,1}$ and $a_{2,1}^*$ have been duplicated. (c) Bottom $a_{2,1}$ and top $a_{2,1}^*$ have been eliminated. (d) Self-loops have been eliminated. (e) $a_{2,1}$ and $a_{2,1}^*$ have been eliminated. (f) $B_{2,1}^*$ has been split, where $B_{2,1}^{*\prime} + B_{2,1}^{*\prime\prime} = B_{2,1}^*$. (g) $B_{2,1}^{*\prime\prime}$ has been eliminated. (h) Self-loop has been eliminated. (i) $B_{2,1}^{*\prime}$ has been eliminated. This leads to the SFG in Fig. 10(c).

$|B_{2,1}|^2$ gives the power presented to the load by the amplifier, but part of it will be reflected by the load according to (19) unless $\Gamma_{L,1} = 0$. The power absorbed by the load, therefore, is given by

$$P_{L,1}(|A_{1,1}|, \Gamma_{L,1}, \Gamma_{L,1}^*) = |B_{2,1}|^2 - |a_{2,1}|^2$$
$$= |B_{2,1}|^2(1 - \Gamma_{L,1}\Gamma_{L,1}^*). \quad (20)$$

Contrary to its appearance, (20) includes effects of the second harmonic to a degree, as explained in Section III-A. Equation (20) can easily be evaluated using (17) on a $\Gamma_{L,1}$-plane Smith chart to plot power contours.

We first compare load-pull power contours obtained from (20) with those from harmonic-balance simulation (see Figs. 11 and 12). We use an amplifier model "RF_PA_CKT" built into ADS [31]. Its small-signal gain is about 29.5 dB, and the input 1-dB gain compression point (IP$_{1dB}$) with a 50-Ω load is about -16.5 dBm. The available power of the signal source is set to $P_{avs} = \{-40, -16.5\}$ dBm with the source impedance being $Z_s = R_{ref} = 50\ \Omega$. X-parameters are "measured" at these input power levels with $Z_L = R_{ref} = 50\ \Omega$, and then, load-pull simulation is performed. The contours in Figs. 11 and 12 are drawn at the same power levels for the closed-form approximation (in red) and simulation (in blue). Fig. 11 shows the small-signal case ($B_{2,1}^{LSOP} \to 0$,

$X_{2,1;2,1}^{(S)} \to S_{22}$, and $X_{2,1;2,1}^{(T)} \to 0$ [11]), and the optimum load impedance is given simply by $\Gamma_{L,1} = X_{2,1;2,1}^{(S)*} = S_{22}^*$ [22]. In the large-signal case (see Fig. 12), the red and blue contours almost overlap near the origin, whereas they tend to separate far from the origin. This is because $a_{2,1}$ and $b_{2,1}$ go to 0 at the origin, whereas the assumption that (19) is small becomes invalid as $\Gamma_{L,1}$ moves farther from the origin. The predicted optimum load reflection coefficient (red circular dot) is consistent with the prediction by Root et al. [22] and is reasonably close to the simulated optimum point. The prediction could, therefore, be useful for establishing a quick initial design [21].

Next, we use measured X-parameters of the amplifier ZFL-11AD+ and compare load-pull contours given by (20) and those from analytic equations (6)–(18) of [20]. The small-signal gain of ZFL-11AD+ is about 11 dB. Since the two sets of equations are derived from the same theoretical starting point (18) with the same set of X-parameters, the resulting two sets of contours are expected to agree with each other. Fig. 13 shows that this is indeed the case. The level of accuracy offered by equations derived using SFGs is the same as that offered by equations derived algebraically. Our result (20) for the power absorbed by the load as a function of $\Gamma_{L,1}$ is much simpler than (6)–(18) of [20] and might be easier to use.

Finally, Fig. 14 compares measured load-pull power contours with approximate load-pull contours from (20). The measurement was made with an Agilent N5245A network analyzer and a Maury MT982AL02 passive load-pull tuner. The agreement is reasonable near the origin.

V. Conclusion and Prospects

We showed, in X-parameter parlance, how to draw SFGs for weakly nonlinear microwave circuits operating around an LSOP. The differences between such SFGs from those for linear circuits are that: 1) the negative-frequency graph needs to be drawn explicitly [see Fig. 4(b)]; 2) branches associated with $X_{p,k;q,l}^{(T)}$ and $X_{p,k;q,l}^{(T)*}$ connect the positive- and negative-frequency graphs [see Fig. 4(c)]; and 3) the first term of (9), representing the LSOP, and its complex conjugate need to be included as source nodes [see Fig. 10(b)]. We also pointed out that $X_{p,k;q,l}^{(T)}$ and $X_{p,k;q,l}^{(T)*}$ could be understood as representing implicit frequency mixing processes, related to intermodulation distortion. The highest frequency involved in such a process is not $k\omega_0$ or $l\omega_0$ but $(k + l)\omega_0$ (see Table I). SFGs thus drawn can be treated in the same way as ordinary SFGs and can, in principle, be used to derive closed-form expressions in terms of X-parameters by using the known techniques [4], [5], [6], [7], [8]. Although SFGs can easily get very complicated, branches associated with very small magnitudes of X-parameters could be pruned before attempting any derivation. Table I and Fig. 7 suggest that $X_{p,k;q,l}^{(T)}$ involving the third or fourth harmonic ($k+l \geq 3$) could be candidates for pruning. A measurement-based decision of which X-parameters to drop (i.e., model order reduction) is described in [14]. Computational aspects of SFGs were studied in [42]. Even when no attempt is made to derive expressions, SFGs offer revealing insights into small-signal responses of weakly nonlinear circuits operating around an LSOP.

As an application example, we derived the output power expression [see (20)] of an amplifier (see Fig. 10) as a function of the load reflection coefficient $\Gamma_{L,1}$ and used it to plot

approximate load-pull power contours (see Figs. 11–14). The approximation was accurate near the center of an R_{ref}-centered Smith chart, but it tended to deteriorate far from the center because of the small-signal assumption of $a_{2,1}$ and $a_{2,1}^*$ in Fig. 10(b). This was a known limitation of load-independent X-parameters. If the optimum load reflection coefficient turns out to lie far from the center of the Smith chart, the region of validity can and should be shifted by choosing a different value of load impedance that defines the LSOP [19], [20], [24]. In this load-dependent case, the LSOP term of (9) becomes dependent on $A_{2,1}$ (or on $\Gamma_{L,1}$ via $A_{2,1} = \Gamma_{L,1}B_{2,1}$ [11], [15], [16], [23]) as follows:

$$B_{p,k}^{\text{LSOP}}(A_{1,1}, A_{2,1}) = X_{p,k}^{(B)}(|A_{1,1}|, A_{2,1}\Phi^{-2})\Phi^k. \qquad (21)$$

SFGs should remain valid in such load-dependent cases too (see Appendix C).

Apart from amplifiers, waveform shaping [43] for oscillators [44] might also be a possible situation where analysis using SFGs could turn out useful. Given the fact that both positive and negative frequencies appear in an SFG for X-parameters, it could also be interesting to apply SFGs to such circuits as complex filters, which have different responses for positive and negative frequencies.

Other possible application areas of SFGs include metrology, especially uncertainty analysis for S-parameter measurement considering weak nonlinearity of passive test fixtures [45], [46], electronic calibration kits [28], or VNA receivers [47], [48]. For example, to account for VNA receiver nonlinearity, its source-dependent X-parameters should be measured in advance. When measuring the S-parameters of a device under test, the power that enters the VNA receiver needs to be measured as well [49]. Using these data, analytic uncertainty propagation could be carried out with the help of an SFG.

Appendix

A. Derivation of the SFG in Fig. 10(c)

Fig. 15 illustrates step-by-step derivation of the SFG shown in Fig. 10(c) by topological manipulation [6], [7]. A redrawn version of the SFG in Fig. 10(b) is shown in Fig. 15(a). Starless (positive-frequency) nodes are on the left-hand side, and starred (negative-frequency) nodes are on the right-hand side. Notice its resemblance to an SFG for a linear two-port with source and load terminations. S-type X-parameters connect nodes on the same side like reflection coefficients, and T-type X-parameters connect nodes on opposite sides like transmission coefficients. The rest of Fig. 15 should be self-explanatory.

B. Small-Signal Output Reflection Coefficient of Amplifier

To look further at the implication of Fig. 10(b) or Fig. 15(a), let us transform the SFG as shown in Fig. 16(a) using (12). Note that

$$b_{2,1} = B_{2,1} - B_{2,1}^{\text{LSOP}} \qquad (22)$$

and, from (19),

$$a_{2,1} = \Gamma_{L,1}B_{2,1}^{\text{LSOP}} + \Gamma_{L,1}b_{2,1}. \qquad (23)$$

A plot of $b_{2,1}$ using (22) and (17) is shown in Fig. 17 in red for $|\Gamma_{L,1}| = 0.1$ and $\angle\Gamma_{L,1}$ swept between $\pm180°$. It shows an
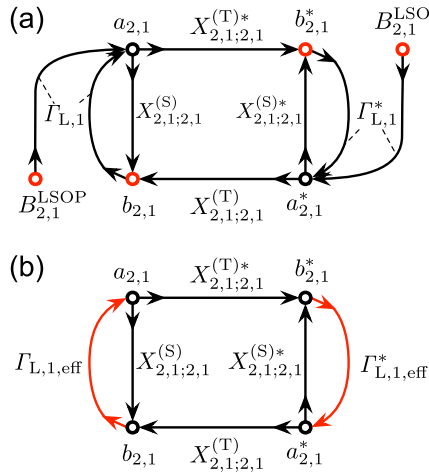
Fig. 16. (a) $B_{2,1}$ and $B_{2,1}^*$ in Fig. 15(a) have been split by using (12). (b) Source nodes $B_{2,1}^{\mathrm{LSOP}}$ and $B_{2,1}^{\mathrm{LSOP}*}$ have been absorbed into $\Gamma_{\mathrm{L},1,\mathrm{eff}}$ and $\Gamma_{\mathrm{L},1,\mathrm{eff}}^*$, respectively.
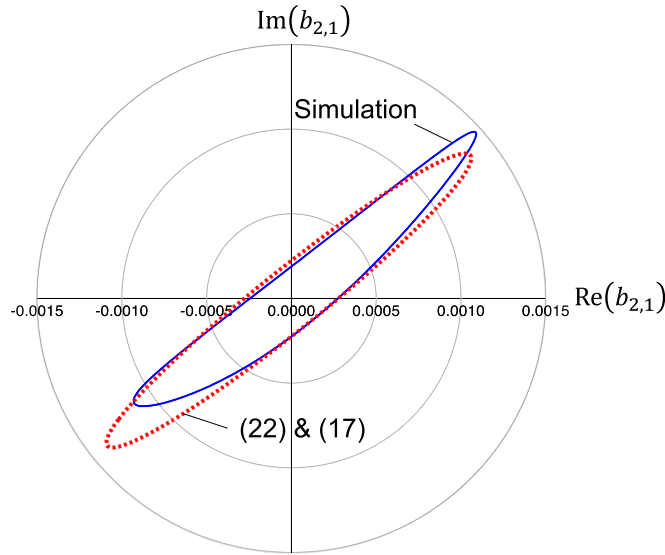

Fig. 17. Red dotted line shows $b_{2,1}$ plotted using (22) and (17) with $|\Gamma_{\mathrm{L},1}| = 0.1$ and $\angle\Gamma_{\mathrm{L},1}$ swept between $\pm 180°$. The X-parameters are those of "RF_PA_CKT" at $P_{\mathrm{avs}} = -18$ dBm. Shown in blue is the harmonic-balance simulation result. This figure corresponds to the middle left plot of Fig. 3.18 of [11], which shows much smaller values of $|b_{2,1}|$.

ellipse as it should [11]. A harmonic-balance simulation result is also shown in Fig. 17. The discrepancy between the analytic result (red) and the simulation result (blue) is presumably due to the facts that X-parameters involving harmonic numbers greater than 1 are not taken into consideration in (17), and that (9) is only a first-order Taylor expansion at the LSOP. The results actually agree better if $|\Gamma_{\mathrm{L},1}|$ or the input power, P_{avs}, is reduced.

Let us introduce, using (22) and (23), an effective load reflection coefficient, $\Gamma_{\mathrm{L},1,\mathrm{eff}}$, around the LSOP as follows:

$$\Gamma_{\mathrm{L},1,\mathrm{eff}} \triangleq \frac{a_{2,1}}{b_{2,1}} = \Gamma_{\mathrm{L},1}\left(1 + \frac{B_{2,1}^{\mathrm{LSOP}}}{b_{2,1}}\right). \qquad (24)$$

The magnitude of $\Gamma_{\mathrm{L},1,\mathrm{eff}}$ may very well (and usually does) exceed unity ($|\Gamma_{\mathrm{L},1,\mathrm{eff}}| \to \infty$ at the LSOP) even if the load is passive ($|\Gamma_{\mathrm{L},1}| \leq 1$) because the second term of (24) is not a property of the load. By using $\Gamma_{\mathrm{L},1,\mathrm{eff}}$, we can reduce the SFG in Fig. 16(a) to the one shown in Fig. 16(b). If we define the
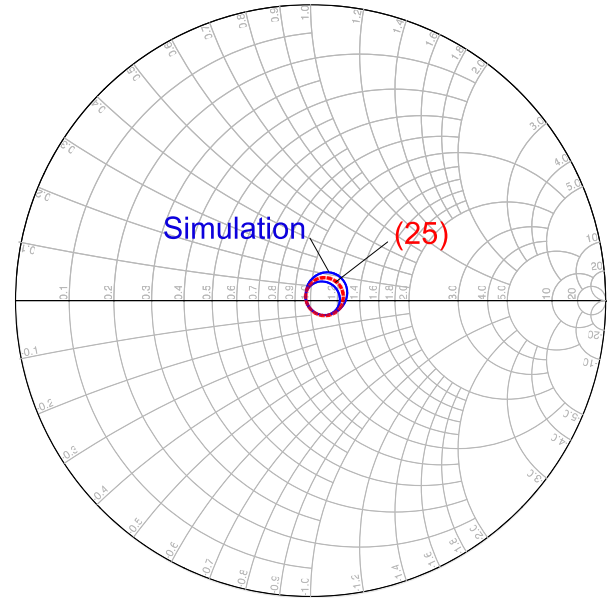

Fig. 18. Red dotted line shows the small-signal output reflection coefficient, $\Gamma_{\mathrm{out},1,\mathrm{ss}}$, of "RF_PA_CKT," plotted using (25) with $|\Gamma_{\mathrm{L},1}| = 0.1$ and $\angle\Gamma_{\mathrm{L},1}$ swept between $\pm 180°$. The X-parameters are the same as in Fig. 17. The unicursal double circle shown in blue is the harmonic-balance simulation result. This figure corresponds to the bottom plot of Fig. 3.18 of [11].

small-signal output reflection coefficient of the amplifier (see Fig. 10(a)) around the LSOP by $\Gamma_{\mathrm{out},1,\mathrm{ss}} \triangleq b_{2,1}/a_{2,1}$, it can be written in terms of X-parameters, by inspection of Fig. 16(b), as

$$\Gamma_{\mathrm{out},1,\mathrm{ss}} = X_{2,1;2,1}^{(S)} + \frac{X_{2,1;2,1}^{(T)}\Gamma_{\mathrm{L},1,\mathrm{eff}}^* X_{2,1;2,1}^{(T)*}}{1 - X_{2,1;2,1}^{(S)*}\Gamma_{\mathrm{L},1,\mathrm{eff}}^*}. \qquad (25)$$

The second term of (25) represents the effect of third-order intermodulation (see Section III-A). Eqation (25) actually depends on $\Gamma_{\mathrm{L},1}^*$, which is a property of the load, via (17), (22), and (24). This dependence on $\Gamma_{\mathrm{L},1}^*$ implies that "the output reflection coefficient is not an intrinsic property of the nonlinear amplifier under large-signal drive" [11, p. 71]. A plot of $\Gamma_{\mathrm{out},1,\mathrm{ss}}$ for $|\Gamma_{\mathrm{L},1}| = 0.1$ and $\angle\Gamma_{\mathrm{L},1}$ swept between $\pm 180°$ is shown in Fig. 18 in red. The fact that it does not show a single point indicates that $\Gamma_{\mathrm{out},1,\mathrm{ss}}$ depends on $\angle\Gamma_{\mathrm{L},1}$. The simulation result in blue exhibits a unicursal double circle. Again, the results will agree better if $|\Gamma_{\mathrm{L},1}|$ or P_{avs} is reduced, and then, the double circle will look like a single circle.

Recently, a superconductive arbitrary waveform synthesizer (a nonlinear one-port network) was characterized using X-parameters [50]. Its "simplified" SFG was shown [50, Fig. 5], in which T-type X-parameters were not incorporated. Its output impedance was estimated using the following approximate formula [50, eq. (7)]:

$$Z_{\mathrm{out}} \approx R_{\mathrm{ref}}\frac{1 + X_{1,1;1,1}^{(S)}}{1 - X_{1,1;1,1}^{(S)}}. \qquad (26)$$

This is equivalent to taking only the first term of (25) (with all port indices renumbered to 1). A better estimate might be obtained by using

$$Z_{\mathrm{out}} = R_{\mathrm{ref}}\frac{1 + \Gamma_{\mathrm{out},1,\mathrm{ss}}}{1 - \Gamma_{\mathrm{out},1,\mathrm{ss}}}. \qquad (27)$$
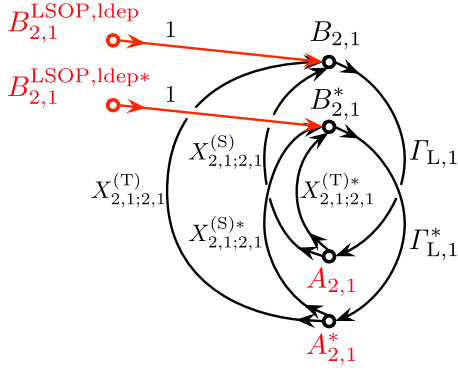
Fig. 19. Load-dependent X-parameter version of the SFG in Fig. 10(b). $\Phi = 1$ is assumed.

Fig. 20. Same as Fig. 12, except that the red contours are plotted using X-parameters obtained with a load impedance of $Z_{\mathrm{L},1}^{\mathrm{LSOP}} = 65 - j15 \ \Omega$.

C. SFGs for Load-Dependent X-Parameters

The SFG theory developed in this article assumed that the load impedance $Z_{\mathrm{L},1}^{\mathrm{LSOP}}$ that defines the LSOP, at which X-parameters are to be measured, is equal to the reference resistance R_{ref}. The assumption led to $A_{q,l}^{\mathrm{LSOP}} = 0$ in (8) for $(q,l) \neq (1,1)$. The theory should be applicable as-is to load-dependent X-parameters, provided that R_{ref} (or, more generally, the reference impedance Z_{ref}) is shifted correspondingly so that $\Gamma_{L,k} = 0$ holds at the LSOP [see (5)]. However, the use of complex reference impedances can be confusing and error-prone [30], [51]. Alternatively, the standard 50-Ω-referenced load-dependent X-parameters can be accommodated as follows.

The first term of (7) becomes

$$B_{p,k}^{\mathrm{LSOP}}\big(A_{1,1}, \Gamma_{\mathrm{L},1}^{\mathrm{LSOP}}\big) = X_{p,k}^{(B)}\big(|A_{1,1}|, \Gamma_{\mathrm{L},1}^{\mathrm{LSOP}}\big)\Phi^k \qquad (28)$$

where $\Gamma_{\mathrm{L},1}^{\mathrm{LSOP}}$ is the load reflection coefficient (at the fundamental tone, ω_0) that establishes the LSOP. Since, generally, $\Gamma_{\mathrm{L},1}^{\mathrm{LSOP}} \neq 0$ in the load-dependent case, $A_{2,1}^{\mathrm{LSOP}} \triangleq \Gamma_{\mathrm{L},1}^{\mathrm{LSOP}} B_{2,1}^{\mathrm{LSOP}} = 0$ no longer holds in (8). Then, nonzero $A_{2,1}^{\mathrm{LSOP}}$ must be incorporated into (18) (with Φ revived) as follows [11, Sec. 5.3]:

$$B_{2,1} = B_{2,1}^{\mathrm{LSOP}} + X_{2,1;2,1}^{(S)}\big(A_{2,1} - A_{2,1}^{\mathrm{LSOP}}\big)$$
$$+ X_{2,1;2,1}^{(T)}\big(A_{2,1}^{*} - A_{2,1}^{\mathrm{LSOP}*}\big)\Phi^2. \qquad (29)$$

The right-hand side can be written as follows:

$$B_{2,1} = B_{2,1}^{\mathrm{LSOP,ldep}} + X_{2,1;2,1}^{(S)}A_{2,1} + X_{2,1;2,1}^{(T)}A_{2,1}^{*}\Phi^2 \qquad (30)$$

where

$$B_{2,1}^{\mathrm{LSOP,ldep}} \triangleq B_{2,1}^{\mathrm{LSOP}} - X_{2,1;2,1}^{(S)}A_{2,1}^{\mathrm{LSOP}}$$
$$- X_{2,1;2,1}^{(T)}A_{2,1}^{\mathrm{LSOP}*}\Phi^2 \qquad (31)$$

is the constant source term for a given LSOP, just as the first term of (9) in the load-independent case. Comparison of (18) and (30) suggests that the load-dependent counterpart of Fig. 10(b) is as shown in Fig. 19. Thus, the load-dependent version of (17) is obtained by the simple substitution $B_{2,1}^{\mathrm{LSOP}} \rightarrow B_{2,1}^{\mathrm{LSOP,ldep}}$. Equation (7) can then
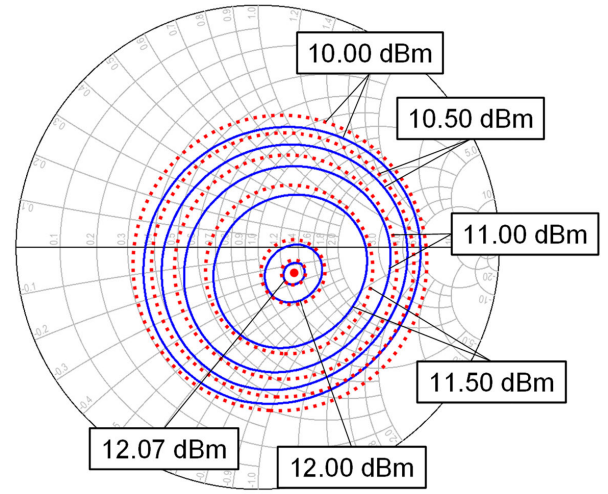
be rewritten as follows:

$$B_{p,k} \simeq B_{p,k}^{\mathrm{LSOP,ldep}} + \sum_{q,l}\Bigg[\frac{\partial X_{p,k}^{(B)}}{\partial(A_{q,l}\Phi^{-l})}\bigg|_{\mathrm{LSOP}} A_{q,l}\Phi^{k-l}$$
$$+ \frac{\partial X_{p,k}^{(B)}}{\partial(A_{q,l}\Phi^{-l})^{*}}\bigg|_{\mathrm{LSOP}} A_{q,l}^{*}\Phi^{k+l}\Bigg] \qquad (32)$$

Equation (32) might not look quite like a Taylor expansion around the LSOP, but it is because of the second and the third terms of (31).

Fig. 20 shows load-pull power contours from harmonic-balance simulation (blue, same as in Fig. 12) and those (red) from (20) with X-parameters obtained with a load impedance of $Z_{\mathrm{L},1}^{\mathrm{LSOP}} = 65 - j15 \ \Omega$ (at the peak output power). The agreement is better around the $Z_{\mathrm{L},1}^{\mathrm{LSOP}}$ than in Fig. 12.

ACKNOWLEDGMENT

REFERENCES

[1] P. Wambacq and W. Sansen, *Distortion Analysis of Analog Integrated Circuits*. Alphen aan den Rijn, The Netherlands: Kluwer, 1998.

[2] S. C. Cripps, "A theory for the prediction of GaAs FET load-pull power contours," in *IEEE MTT-S Int. Microw. Symp. Dig.*, May 1983, pp. 221–223, doi: 10.1109/MWSYM.1983.1130864.

[3] S. C. Cripps, *RF Power Amplifiers for Wireless Communications*, 2nd ed. Norwood, MA, USA: Artech House, 2006.

[4] S. J. Mason, "Feedback theory—Some properties of signal flow graphs," *Proc. IRE*, vol. 41, no. 9, pp. 1144–1156, Sep. 1953, doi: 10.1109/JRPROC.1953.274449.

[5] S. J. Mason, "Feedback theory—Further properties of signal flow graphs," *Proc. IRE*, vol. 44, no. 7, pp. 920–926, Jul. 1956, doi: 10.1109/JRPROC.1956.275147.

[6] N. Kuhn, "Simplified signal flow graph analysis," *Microw. J.*, vol. 6, no. 11, pp. 59–66, Nov. 1963.

[7] R. E. Collin, *Foundations for Microwave Engineering*, 2nd ed. Hoboken, NJ, USA: Wiley, 2001.

[8] R. Mavaddat, *Network Scattering Parameters*. Singapore: World Scientific, 1996.

[9] J. Verspecht, D. F. Williams, D. Schreurs, K. A. Remley, and M. D. McKinley, "Linearization of large-signal scattering functions," *IEEE Trans. Microw. Theory Techn.*, vol. 53, no. 4, pp. 1369–1376, Apr. 2005, doi: 10.1109/TMTT.2005.845771.

[10] D. E. Root, J. Verspecht, D. Sharrit, J. Wood, and A. Cognata, "Broadband poly-harmonic distortion (PHD) behavioral models from fast automated simulations and large-signal vectorial network measurements," *IEEE Trans. Microw. Theory Techn.*, vol. 53, no. 11, pp. 3656–3664, Nov. 2005, doi: 10.1109/TMTT.2005.855728.

[11] D. E. Root, J. Verspecht, J. Horn, and M. Marcu, *X-parameters: Characterization, Modeling, and Design of Nonlinear RF and Microwave Components*. Cambridge, U.K.: Cambridge Univ. Press, 2013.

[12] C. Baylis, R. J. Marks, J. Martin, H. Miller, and M. Moldovan, "Going nonlinear," *IEEE Microw. Mag.*, vol. 12, no. 2, pp. 55–64, Apr. 2011, doi: 10.1109/MMM.2010.940102.

[13] M. Myslinski, F. Verbeyst, M. V. Bossche, and D. Schreurs, "S-functions extracted from narrow-band modulated large-signal network analyzer measurements," in *Proc. 74th ARFTG Microw. Meas. Conf.*, Nov. 2009, pp. 1–8, doi: 10.1109/ARFTG74.2009.5439100.

[14] M. Myslinski, F. Verbeyst, M. Vanden Bossche, and D. Schreurs, "S-functions behavioral model order reduction based on narrowband modulated large-signal network analyzer measurements," in *Proc. 75th ARFTG Microw. Meas. Conf.*, May 2010, pp. 1–6, doi: 10.1109/ARFTG.2010.5496321.

[15] G. Simpson, J. Horn, D. Gunyan, and D. E. Root, "Load-pull + NVNA = enhanced X-parameters for PA designs with high mismatch and technology-independent large-signal device models," in *Proc. 72nd ARFTG Microw. Meas. Symp.*, Dec. 2008, pp. 88–91, doi: 10.1109/ARFTG.2008.4804301.

[16] J. Horn, D. E. Root, and G. Simpson, "GaN device modeling with X-parameters," in *Proc. IEEE Compound Semiconductor Integr. Circuit Symp. (CSICS)*, Oct. 2010, pp. 1–4, doi: 10.1109/CSICS.2010.5619691.

[17] A. M. Pelaez-Perez, J. I. Alonso, M. Fernandez-Barciela, A. Rodriguez-Testera, P. J. Tasker, and S. Woodington, "Experimental verification of analytical design equations based on X-parameters for predicting role of series feedback," in *Proc. Eur. Microw. Integr. Circuits Conf.*, Oct. 2011, pp. 148–151.

[18] A. M. Pelaez-Perez, S. Woodington, J. I. Alonso, M. Fernandez-Barciela, and P. J. Tasker, "X-parameters-based closed-form expressions for evaluating power-dependent fundamental negative and positive real impedance boundaries in oscillator design," *IET Microw., Antennas Propag.*, vol. 6, no. 8, pp. 835–840, 2012, doi: 10.1049/iet-map.2011.0373.

[19] A. M. Pelaez-Perez, S. Woodington, M. Fernández-Barciela, P. J. Tasker, and J. I. Alonso, "Large-signal oscillator design procedure utilizing analytical X-parameters closed-form expressions," *IEEE Trans. Microw. Theory Tech.*, vol. 60, no. 10, pp. 3126–3136, Oct. 2012, doi: 10.1109/TMTT.2012.2209436.

[20] A. M. Pelaez-Perez, S. Woodington, M. Fernandez-Barciela, P. J. Tasker, and J. I. Alonso, "Application of an NVNA-based system and load-independent X-parameters in analytical circuit design assisted by an experimental search algorithm," *IEEE Trans. Microw. Theory Techn.*, vol. 61, no. 1, pp. 581–586, Jan. 2013, doi: 10.1109/TMTT.2012.2226056.

[21] M. Fernandez-Barciela, A. M. Pelaez-Perez, S. Woodington, J. I. Alonso, and P. J. Tasker, "Stretching the design: Extending analytical circuit design from the linear to the nonlinear domain," *IEEE Microw. Mag.*, vol. 15, no. 6, pp. 106–120, Sep./Oct. 2014, doi: 10.1109/MMM.2014.2332851.

[22] D. E. Root, J. Verspecht, and J. Xu, "Closed-form solutions to large-signal PA problems: Wirtinger calculus applied to X-parameter," in *Proc. 12th Eur. Microw. Integr. Circuits Conf. (EuMIC)*, Oct. 2017, pp. 212–215, doi: 10.23919/EuMIC.2017.8230697.

[23] B. Pichler and H. Arthaber, "Solution for the large-signal matching problem: Maximizing the efficiency using X-parameters," in *Proc. Int. Workshop Integr. Nonlinear Microw. Millimetre-Wave Circuits*, Jul. 2020, pp. 1–3, doi: 10.1109/INMMiC46721.2020.9160069.

[24] H. G. Joujili, M. Mivehchy, and M. Habibi, "A novel analytical design approach for determining the optimum load to minimize harmonic output power based on X-parameters," *IEEE Trans. Microw. Theory Techn.*, vol. 64, no. 11, pp. 3492–3500, Nov. 2016, doi: 10.1109/TMTT.2016.2604804.

[25] R. Essaadali, A. Jarndal, A. B. Kouki, and F. M. Ghannouchi, "A new GaN HEMT equivalent circuit modeling technique based on X-parameters," *IEEE Trans. Microw. Theory Techn.*, vol. 64, no. 9, pp. 2758–2777, Sep. 2016, doi: 10.1109/TMTT.2016.2594234.

[26] R. Essaadali, A. Jarndal, A. B. Kouki, and F. M. Ghannouchi, "On the accurate voltage and current analytical relationship to X-parameters of a nonlinear two-port network," *IEEE Trans. Microw. Theory Tech.*, vol. 66, no. 10, pp. 4439–4451, Oct. 2018, doi: 10.1109/TMTT.2018.2863231.

[27] R. Essaadali, A. Jarndal, A. B. Kouki, and F. M. Ghannouchi, "Conversion rules between X-parameters and linearized two-port network parameters for large-signal operating conditions," *IEEE Trans. Microw. Theory Techn.*, vol. 66, no. 11, pp. 4745–4756, Nov. 2018, doi: 10.1109/TMTT.2018.2863227.

[28] J. P. Dunsmore, *Handbook of Microwave Component Measurements With Advanced VNA Techniques*, 2nd ed. Hoboken, NJ, USA: Wiley, 2020.

[29] R. B. Marks and D. F. Williams, "A general waveguide circuit theory," *J. Res. Nat. Inst. Standards Technol.*, vol. 97, no. 5, pp. 533–562, Oct. 1992, doi: 10.6028/jres.097.024.

[30] S. Amakawa, "Scattered reflections on scattering parameters—Demystifying complex-referenced S parameters," *IEICE Trans. Electron.*, vol. E99.C, no. 10, pp. 1100–1112, 2016, doi: 10.1587/transele.E99.C.1100.

[31] *Advanced Design System (ADS)*, Keysight Technol., Santa Rosa, CA, USA, 2021.

[32] J. C. Pedro, "The wonderful world of nonlinearity: A distinguished microwave lecture on the modeling and characterization of RF and microwave circuits," *IEEE Microw. Mag.*, vol. 16, no. 9, pp. 22–35, Oct. 2015, doi: 10.1109/MMM.2015.2453871.

[33] A. M. Teetzel, "Two plus two equals four? Maybe not: A tutorial on the graphical analysis of complex signals," *IEEE Microw. Mag.*, vol. 17, no. 9, pp. 32–44, Sep. 2016, doi: 10.1109/MMM.2016.2576959.

[34] P. J. Schreier and L. L. Scharf, *Statistical Signal Processing of Complex-Valued Data*. Cambridge, U.K.: Cambridge Univ. Press, 2010.

[35] Y. Hoshina, "Signal flow graphs of nonlinear or time-varying circuits in terms of X-parameters," Graduation thesis, Fac. Eng., Hiroshima Univ., Higashihiroshima, Japan, Mar. 2021.

[36] S. Amakawa, S. Lee, K. K. Tokgoz, and H. Ito, "Visualizing small-signal responses of a nonlinear RF circuit under large-signal operating conditions," in *Proc. Int. Symp. Biomed. Eng.*, Dec. 2021, pp. 188–189.

[37] R. M. Biernacki, M. Marcu, and D. E. Root, "Circuit optimization with X-parameter models," in *IEEE MTT-S Int. Microw. Symp. Dig.*, Jun. 2017, pp. 1498–1500, doi: 10.1109/MWSYM.2017.8058908.

[38] L. Chua, "Device modeling via nonlinear circuit elements," *IEEE Trans. Circuits Syst.*, vol. CS-27, no. 11, pp. 1014–1044, Nov. 1980, doi: 10.1109/TCS.1980.1084742.

[39] H. Qi, J. Benedikt, and P. J. Tasker, "Nonlinear data utilization: From direct data lookup to behavioral modeling," *IEEE Trans. Microw. Theory Techn.*, vol. 57, no. 6, pp. 1425–1432, Jun. 2009, doi: 10.1109/TMTT.2009.2019996.

[40] B. Pichler, G. Magerl, and H. Arthaber, "A study on quadratic PHD models for large signal applications," *IEEE Trans. Microw. Theory Techn.*, vol. 67, no. 7, pp. 2514–2520, Jul. 2019, doi: 10.1109/TMTT.2019.2915086.

[41] C. Wilson, A. Zhu, J. Cai, and J. B. King, "Pade-approximation based behavioral modeling for RF power amplifier design," *IEEE Access*, vol. 9, pp. 18904–18914, 2021, doi: 10.1109/ACCESS.2021.3052687.

[42] P. Wambacq, G. G. E. Gielen, and W. Sansen, "Symbolic network analysis methods for practical analog integrated circuits: A survey," *IEEE Trans. Circuits Syst. II, Analog Digit. Signal Process.*, vol. 45, no. 10, pp. 1331–1341, Oct. 1998, doi: 10.1109/82.728846.

[43] P. J. Tasker, "Practical waveform engineering," *IEEE Microw. Mag.*, vol. 10, no. 7, pp. 65–76, Dec. 2009, doi: 10.1109/MMM.2009.934518.

[44] R. Kananizadeh and O. Momeni, "High-power and high-efficiency millimeter-wave harmonic oscillator design, exploiting harmonic positive feedback in CMOS," *IEEE Trans. Microw. Theory Techn.*, vol. 65, no. 10, pp. 3922–3936, Oct. 2017, doi: 10.1109/TMTT.2017.2690291.

[45] A. P. Shitvov, D. S. Kozlov, and A. G. Schuchinsky, "Nonlinear characterization for microstrip circuits with low passive intermodulation," *IEEE Trans. Microw. Theory Techn.*, vol. 66, no. 2, pp. 865–874, Feb. 2018, doi: 10.1109/TMTT.2017.2758726.

[46] Q. Jin, J. Gao, G. T. Flowers, Y. Wu, G. Xie, and L. Bi, "Modeling of passive intermodulation in connectors with coating material and iron content in base brass," *IEEE Trans. Microw. Theory Techn.*, vol. 67, no. 4, pp. 1346–1356, Apr. 2019, doi: 10.1109/TMTT.2019.2893193.

[47] W. V. Moer and L. Gomme, "NVNA versus LSNA: Enemies or friends?" *IEEE Microw. Mag.*, vol. 11, no. 1, pp. 97–103, Feb. 2010, doi: 10.1109/MMM.2009.935213.

[48] A. C. Stelson, A. M. Hagerstrom, J. A. Jargon, and C. J. Long, "Quantifying receiver nonlinearities in VNA measurements for the WR-15 waveguide band," *IEEE Trans. Microw. Theory Techn.*, vol. 70, no. 5, pp. 2743–2749, May 2022, doi: 10.1109/TMTT.2022.3155466.

[49] A. Ferrero and U. Pisani, "An improved calibration technique for on-wafer large-signal transistor characterization," *IEEE Trans. Instrum. Meas.*, vol. 42, no. 2, pp. 360–364, Apr. 1993, doi: 10.1109/19.278582.

[50] A. S. Boaventura et al., "Cryogenic characterization of a superconductor quantum-based microwave reference source for communications and quantum information," *IEEE Trans. Appl. Supercond.*, vol. 31, no. 9, pp. 1–9, Dec. 2021, doi: 10.1109/TASC.2021.3117610.

[51] S. Amakawa, "How does my microwave/EM simulator define complex-referenced S-parameters?" in *Proc. Vietnam-Japan Microw.*, Jun. 2017, pp. 112–115. [Online]. Available: https://home.hiroshima-u.ac.jp/amakawa/files/Amakawa_hdmmsdcrsp.pdf

Shuhei Amakawa (Member, IEEE) received the B.Eng., M.Eng., and Ph.D. degrees from The University of Tokyo, Tokyo, Japan, in 1995, 1997, and 2001, respectively, and the M.Phil. degree in physics from the University of Cambridge, Cambridge, U.K., in 2000.

He was a Research Fellow at the Cavendish Laboratory, University of Cambridge, from 2001 to 2004. After working for Silvaco and Cadence, he joined the Tokyo Institute of Technology, Tokyo, in 2006. Since 2010, he has been with Hiroshima University, Higashihiroshima, Japan, where he is currently a Professor at the Graduate School of Advanced Science and Engineering. He co-founded Device Lab Inc., Tsukuba, Japan. in 2017 and served as its Director until 2021. His research interests include modeling and simulation of nanoelectronic devices and systems, design of RF integrated circuits, and microwave theory and measurement.

Dr. Amakawa is also a Committee Member of the International Solid-State Circuits Conference.

Ryotaro Sugimoto received the B.Eng. degree from Hiroshima University, Higashihiroshima, Japan, in March 2022, where he is currently pursuing the master's degree.

Korkut Kaan Tokgoz (Member, IEEE) received the B.Sc. and M.Sc. degrees from the Electrical and Electronics Engineering Department, Middle East Technical University, Ankara, Turkey, in 2009 and 2012, respectively, and the M.Eng. and Ph.D. degrees from the Department of Physical Electronics, Tokyo Institute of Technology, Tokyo, Japan, in 2014 and 2018, respectively.

From 2018 to 2019, he worked as a Senior Researcher/Assistant Manager at NEC Corporation, Kanagawa, Japan, where he was involved in 5G systems and fixed point-to-point wireless links. From 2019 to 2022, he worked as an Assistant Professor at the Tokyo Institute of Technology. He is currently working as a Faculty Member at the Faculty of Engineering and Natural Sciences, SabancıUniversity, Istanbul, Turkey. He is also the Co-Founder and the CTO of Evrim Company Ltd., Yokohama, Japan. His research interests include analog/RF/millimeter-wave/subterahertz transceivers for wireless communications, low-power edge-AI for monitoring systems, IoT, sensors and systems, deembedding, device characterization, and high-power, high-efficiency power amplifiers (PAs) for wireless systems.

Dr. Tokgoz was a recipient of several awards, scholarships, and grants, including the TUBITAK 2232-B International Fellowship for Early-Stage Researchers in 2022, the Marie Skłodowska-Curie Actions Post-Doctoral Fellowship in 2022, the SSCS Predoctoral Achievement Award in 2018, the IEEE MTT-S Graduate Student Fellowship in 2017, the IEICE Student Encouragement Prize in 2017, the Seiichi Tejima Overseas Student Research Award, and the IEEE/ACM ASP-DAC University LSI Design Contest 2017 Best Design Award.

Sangyeop Lee (Member, IEEE) received the B.E. degree in electrical and electronic engineering from the Tokyo Institute of Technology, Tokyo, Japan, in 2009, and the M.E. and Ph.D. degrees in electronics and applied physics from the Tokyo Institute of Technology, Yokohama, Japan, in 2010 and 2013, respectively.

After working for a Korean research institute, Agency for Defense Development (ADD), Daejeon, South Korea, he was a Researcher and an Assistant Professor with Hiroshima University, Higashihiroshima, Japan, from 2017 to 2020. In 2020, he joined the Tokyo Institute of Technology, Yokohama, where he is currently an Assistant Professor. His current research interests include the design of millimeter-wave/terahertz CMOS circuits and IoT sensors.

Hiroyuki Ito (Member, IEEE) received the B.E. degree from the Department of Electronics and Mechanical Engineering, Chiba University, Chiba, Japan, in 2002, and the M.E. and Ph.D. degrees from the Department of Advanced Applied Electronics, Tokyo Institute of Technology, Yokohama, Japan, in 2004 and 2006, respectively.

He was a Temporary Visiting Researcher and a Visiting Professor with the Communications Technology Laboratory, Intel Corporation, Hillsboro, OR, USA, in 2006 and 2007, respectively. He was an Assistant Professor with the Precision and Intelligence Laboratory, Tokyo Institute of Technology, from 2007 to 2013. From 2008 to 2010, he was with Fujitsu Laboratories Ltd., Yokohama, where he developed an RF CMOS transceiver and digital calibration techniques for mobile-WiMAX applications. From 2013 to 2015, he was an Associate Professor with the Precision and Intelligence Laboratory, Tokyo Institute of Technology. Since 2016, he has been an Associate Professor with the Institute of Innovative Research, Tokyo Institute of Technology. He has been the Co-Founder and the CEO of EVRIM Company Ltd., Yokohama, since 2020. His research interests include ultralow-power RF circuits, high-sensitivity microelectromechanical systems (MEMS) accelerometers, low-noise and crystal-less RF synthesizers, and cow management systems exploiting IoT and deep/machine learning.

Dr. Ito was a Research Fellow of the Japan Society for the Promotion of Science from 2004 to 2007. He is currently an International Technical Program Committee Member of the International Solid-State Circuits Conference. He is also a member of the IEEE Solid-State Circuits Society, the Institute of Electronics, Information and Communication Engineers (IEICE), the Japan Society of Applied Physics (JSAP), and the Japanese Society of Agricultural Machinery and Food Engineers. He was a recipient of the European Solid-State Circuits Conference (ESSCIRC) 2008 Best Paper Award.

Ryoko Kishikawa received the B.E. degree in physics from Kyoto University, Kyoto, Japan, in 2008, the M.S. degree in condensed matter physics from Tokyo University, Tokyo, Japan, in 2010, and the Ph.D. degree in physical science from the Graduate University for Advanced Studies (Soukendai), Kanagawa, Japan, in 2018.

Since 2010, she has been a Research Scientist with the National Institute of Advanced Industrial Science and Technology (AIST), Tsukuba, Japan. Her main research interest is a measurement technique for passive and active devices from radio frequency to submillimeter frequency.